Journal of Materials Chemistry A

Accepted Manuscript

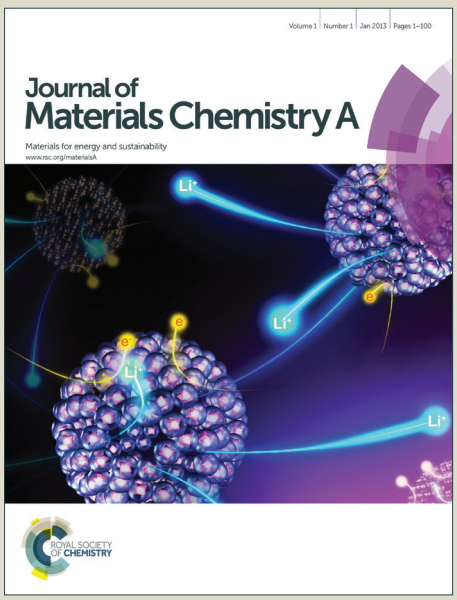

ROYAL SOCIETY OF CHEMISTRY

www.rsc.org/materialsA

Enhancing Photocatalytic Activity of Disorder-Engineered C/TiO_2 and TiO_2 Nanoparticles

Shu Wang, Lei Zhao, Lina Bai, Junmin Yan, Qing Jiang, Jianshe Lian*

Key Lab of Automobile Materials, Ministry of Education, College of Materials Science and Engineering, Jilin University, Nanling Campus, Changchun, 130025, P.R. China

Abstract

We demonstrate a simple and green synthetic pathway to prepare TiO_2-carbon nanoparticles (C/TiO_2 NPs) by sol-gel method, abandoning additional carbon sources but utilizing the organic group in Ti precursor. Then the C/TiO_2 NPs were decarburized under air atmosphere at 500°C for 2h to form the reduced TiO_2 nanoparticles. The XRD, Raman spectrum, HRTEM and electron energy loss spectrum (EELS) analyses showed that the C/TiO_2 NPs were the composite of core-shell structured TiO_2 and amorphous carbon; and both C/TiO_2 and reduced TiO_2 NPs contained a large number of oxygen vacancies, which leaded to structural disorders in them. These structural disorders induced the valence band tails to enhance visible light absorption and to tailor the bandgap structures of the two modified TiO_2 samples to match with the hydrogen and oxygen production energy levels. As a result, the two structure-disordered C/TiO_2 and reduced TiO_2 nanocrystals showed excellent solar-driven photocatalytic activities: the C/TiO_2 performed the best on the photodegradation of phenol and methyl blue; while the reduced TiO_2 displayed an excellence in the hydrogen generation rate with 10 times higher than that of the reference TiO_2 by photo-splitting water.

* Corresponding author. E-mail: lianjs@jlu.edu.cn
Tel: 86-431-85095876 Fax: 86-431-85095876

Keywords: nanoparticals; structural disorder; bandgap engineering; photocatalytic activity

Introduction

Semiconductor photocatalysis begins with the activation of photogenerated carriers, and these excited carriers may transfer to the surface to initiate the photocatalytic reactions [1-3]. TiO_2, as a widely used wide band-gap semiconductor, has been extensively studied due to its abundance, nontoxicity, and stability [4-7]. However, the rapid combination of e^-/h^+ pair dominates the photocatalytic reactions and ordinary anatase phase TiO_2 absorbs only ultraviolet light of solar spectrum [8]. For practical applications, there have been mainly two ways to improve the photocatalytic activity of TiO_2, one is prolonging the lifetime of these photo-carriers or suppressing the combination of photogenerated electron-hole pairs, and the other is enhancing of solar energy conversion by band-gap engineering. Therefore, to improve the optical response and photocatalytic activity of TiO_2 in the whole solar spectra range, numerous efforts have been devoted and a certain amount of progress is obtained [9-12]. Recently, two kinds of "black TiO_2" aiming to solve the above problems have been proposed and aroused great attention. One black TiO_2 is the composite of TiO_2 commixing with black-colored carbon species like graphene [13-15]. Several reports on physical black-colored carbon species/TiO_2 composites have confirmed their excellent abilities of photogenerated carrier transfer on improving the photocatalytic activity [16,17]. While lately research has significantly suggested that TiO_2-graphene is in essence the same as other TiO_2-carbon composite materials on enhancement of photocatalytic activity [18]. Another black-colored TiO_2 is an innovative modification of TiO_2 by introducing surface disorder to narrow the bandgap of TiO_2 nanocrystals and to increase the visible and near infrared (Vis-NIR) optical absorption [19-21]. These chemically disorder-engineered TiO_2 nanocrystals greatly adjust the band structure to fit the redox

potential of water in the photocatalytic water-splitting process, thus to possess the ability to produce H_2 with considerable efficiency [19, 21]. Whereas the strategies for preparing "black TiO_2" materials have a number of limitations such as multiple steps, harsh synthesis conditions, or expensive facilities for the modified works [13-22].

In present work, we proposed an economical and green synthetic pathway to use the traditional sol-gel technique, abandoning additional carbon sources but utilizing the organic group in Ti precursor, to prepare nanostructured TiO_2-carbon core-shell composites. These C/TiO_2 nanoparticles (NPs) should have two advantages: the covered carbon layers may support the effective separation of photogenerated electron/hole pairs, and the induced disorders in TiO_2 lattice may improve the visible light response of TiO_2 crystals; hence, the modified TiO_2-carbon composite should exhibit significant advancement on solar-driven photocatalytic performance and provide a simple way to practitioners for semiconductor photocatalyst's modification. Furthermore, we decarburized the TiO_2-carbon composite through annealing it in air to obtain the defect-engineered TiO_2 with only structural disorders, which should also have enhanced photocatalytic performance. The structures of the TiO_2-carbon composite and its decarburization product were characterized and their solar-driven photocatalytic activities in the degradation of organic pollutant (phenol and methyl blue) and H_2 production were investigated.

Preparations

The samples were prepared by sol–gel technique with a typical synthetic procedure. A precursor solution consisting of tetrabutyl titanate, ethanol, hydrochloric acid and deionized water was prepared. Aging the solution for 48 h at room temperature to form gels, the gels were dried at 80°C for 12 h to form dried powder. According to the general sol-gel process, a part of the powder was

calcinated at 500°C in air to form the ordinary TiO_2 powder as a reference sample.

As a modification, nitrogen gas was passed through the quartz tube to dilute oxygen to a proper content, hence the C-rich (called C/TiO_2) powder was obtained by calcinating at 500°C in the N_2 atmosphere. For the C/TiO_2, the carbon layers were obtained by the carbonization of alkoxy (-OC_4H_9) in Ti precursor ($Ti(OC_4H_9)_4$) under the oxygen-lack environment (**S1**). Consequently, the C/TiO_2 was further calcinated at 500°C for 2h in air to form the decarburized TiO_2, called as reduced TiO_2. All the thermal treatments were carried out using a heating rate of 10 °C/min in a tube furnace. So there are three TiO_2 samples: reference TiO_2, C/TiO_2 and reduced TiO_2, respectively, and then their structure characterizations (**S2**) and photocatalytic performances (**S3**) are investigated.

Results and discussion

Fig. 1 shows the XRD patterns of three samples, they are all anatase phase without any other phase detected. The Full Width Half Maximum (FWHM) of the C/TiO_2 and reduced TiO_2 samples are wider than that of the reference TiO_2, which gives the estimation of average grain size by the Scherrer equation to be 23, 9, and 13 nm for reference TiO_2, C/TiO_2 and reduced TiO_2 NPs, respectively. The modified synthetic procedure produces the C/TiO_2 and reduced TiO_2 NPs with much smaller average grain sizes hence with larger surface areas, which should be favorable for photocatalytic performance. The inset figure shows that the estimated lattice strain increases evidently with decreasing average grain size. Refined structural parameters (**Table S1**) calculated from the XRD spectra show no evident volume difference (less than 0.3%) among these powders, so the increased lattice strain (reaching to about 1.3%) is mainly attributed to the severe lattice distortion.

Structural properties of the synthesized TiO_2 are further examined by measuring their Raman

scattering, shown in **Fig. 2**. All the three samples show the anatase TiO_2 vibrational spectrum with six Raman-active fundamentals (Eg(1), Eg(2) and Eg(3) at 141, 192, and 638 cm^{-1}, B1g(1) and B1g(2)) at 395 and 514 cm^{-1}, and A1g mode at 514 cm^{-1}, respectively), indicating the existence of TiO_2 in these samples, which is in agreement with the XRD results. The Raman spectrum of the C/TiO_2 powder is different from those of the other two samples: two intense characteristic peaks of graphite-like carbon, D-band and G-band, centered at 1373 and 1602 cm^{-1}, respectively, appear in the C/TiO_2 sample. The G-band at 1602 cm^{-1} confirms the presence of sp^2 carbon-type structure of the C/TiO_2 particles [23], while the D-band at around 1373 cm^{-1} is attributed to the presence of defects within the hexagonal graphitic structure [16].

Fig. 3(a), (b) and **(c)** show the high resolution TEM (HRTEM) images of the reference TiO_2, C/TiO_2 and reduced TiO_2 NPs, respectively, and their corresponding Fourier-filtered images are displayed as inserts. By contrast, reference TiO_2 shows well arrangement of lattice, while the Fourier-filtered images (insets b1 and c1 in **Fig. 3(b)** and **Fig. 3(c)**, respectively) of the C/TiO_2 and reduced TiO_2 clearly show the severe lattice distortions and some of them develop into dislocations in the selected areas, and the severity of disorders could also be proved by lattice strain calculated in XRD. The located images (insets b2 and b3) clearly show the core-shell morphology of C/TiO_2 with a ~1.5 nm thick of amorphous carbon layer, and the carbon layer totally disappears in the reduced TiO_2 NP after decarburization (shown in insets c2 and c3). The carbon shell acts as barrier on the grain boundary to obstruct the growth of anatase TiO_2 to result in a decrease in crystal size (9 nm). The reduced TiO_2 has a small secondary growth after decarburization (13 nm) according to the XRD calculated grain size.

Electron energy loss near edge structure (ELNES) appears above the absorption edge in the

electron energy loss spectrum (EELS), which is sensitive to the unoccupied valence band and could interpret the electronic states qualitatively. **Fig. 3(d)** shows the comparison of the Ti L-edge ELNES of the EELS spectra (**Fig. S1**) of the three samples. Ti $L_{2;3}$ edges are the main features of the TiO_2 spectrum and allow a qualitative measurement of the chemical state of Ti element. The L_3 and L_2 lines are the transitions from $2p_{3/2}$ to $3d_{3/2}3d_{5/2}$ and from $2p_{1/2}$ to $3d_{3/2}$, respectively, and their intensities are related to the unoccupied states in the 3d bands [24, 25]. From Figure 3(d), the Ti $L_{2;3}$ edges of reference TiO_2, C/TiO_2 and reduced TiO_2 NPs are 463.43 eV vs. 462.15 eV vs. 462.31 eV in L_3 and 468.26 eV vs. 466.96 eV vs. 467.14 eV in L_2, respectively, i.e., a decrease of the chemical state energy of Ti in C/TiO_2 and reduced TiO_2 NPs is observed. For the Ti $L_{2;3}$ edges ELNES, Ti ions with a higher valence would locate at a higher energy edge, therefore, the results demonstrate the average decrease of Ti valence state in both C/TiO_2 and reduced TiO_2 NPs, which implies the mixture of Ti^{4+} with a certain quantity of Ti^{3+} [20]. In fact, the C/TiO_2 and reduced TiO_2 were prepared in an oxygen-lack atmosphere hence should have more oxygen vacancies/V_Os (i.e. TiO_{2-x}), the appearance of Ti^{3+} ions should be normal [26, 27]. The existence of V_Os results in the lattice contraction as testified by the decrease of lattice parameters from the above XRD analysis and the lattice distortion or lattice dislocations from the HRTEM observation. So, the combined consideration of the XRD, HRTEM and EELS studies confirms that the C/TiO_2 and reduced TiO_2 have more V_Os and a certain quantity of Ti^{3+} in their TiO_2 lattices. In addition, the EELS spectrum for C K-edge ELNES of C/TiO_2 proves that the carbon shell exists as amorphous carbon by its ELNES fingerprints shown in **Fig. S1(b)**.

The photocatalytic activities of the three synthesized catalysts were evaluated by the degradation of phenol and methyl blue (MB) solutions using the simulated solar light source (see

detail in **S3**). **Fig. 4(a)** and **Fig. S3** show that both C/TiO_2 and reduced TiO_2 NPs exhibit significant enhancement in solar-driven photocatalytic activity in comparison with the reference TiO_2, and C/TiO_2 shows the best performance: MB was decomposed in 30 min (**Fig. S3**) and phenol was decomposed in 80 min (**Fig. 4(a)**), while only 20% of MB or phenol was decomposed by the reference TiO_2 in the corresponding intervals. The obvious advantage of C/TiO_2 on photo-degradation of MB solution can be attributed to the adsorption of carbon layers to the dye, comparing with the degradation of phenol solution.

The C/TiO_2 and reduced TiO_2 samples also exhibit substantial activity and stability in the photocatalytic production of hydrogen from water-splitting under the simulated solar light, which endow their usability in new energy source filed. 20 mg photocatalyst loaded with 0.6 wt% Pt was placed into a Pyrex glass container filled with the solution of water:methanol (as a sacrificial agent) =1:1 in a closed-gas circulation system, and the generated H_2 was measured. Hydrogen gas evolution as a function of time using three TiO_2 samples as the photocatalysts is shown in **Fig. 4(b)**. The reference TiO_2 displays a stable H_2 release rate of ~0.154 mmol $hour^{-1}$ g^{-1}, while the C/TiO_2 and reduced TiO_2 NPs show evidently increased H_2 release rates of ~0.577 mmol $hour^{-1}$ g^{-1} and ~1.560 mmol $hour^{-1}$ g^{-1}, respectively. That is, the reduced TiO_2 NPs shows the best solar-driven hydrogen production rate through water-splitting among the three TiO_2 NPs, which is about ten times higher than that of the reference TiO_2.

Fig. 5 exhibits the UV-Visible absorption spectra of the three samples. First, the spectra of the samples of C/TiO_2 and reduced TiO_2 shift to a longer wavelength, revealing the decrease in their band gap. The optical band gap of reference TiO_2 is 3.3 eV, while those of C/TiO_2 and reduced TiO_2 are 2.9 eV and 3.2 eV, respectively. The significant bandgap narrowing (2.9 eV) of C/TiO_2 is mainly

attributed to surface C-doping. The C atoms occupying the interstitial sites in TiO_2 lattice normally exist in the TiO_2/carbon species composites [18], which leads to a decrease of optical bandgap energy. In addition, the optical absorbance of reduced TiO_2 in the visible range is obviously enhanced compared to the reference TiO_2, as shown by the inset of **Fig 5**. It is speculated that the TiO_2 in C/TiO_2 should also have enhanced visible light absorbance, although it is covered by the great absorption in visible region of the surface amorphous carbon layer.

Surface chemical bonding of TiO_2 nanocrystals was detected by X-ray photoelectron spectroscopy (XPS) shown in **Fig. S2**. To compare with the experimentally introduced carbon, the strong signal of XP C 1s at 284.8 eV proves the presence of carbon shell in C/TiO_2 NPs shown as Fig. S2 (a). In our work, we attempt to illustrate the reason for C-rich from calcination process in the supporting information of manuscript (S1). Since the content of carbon is considerable, it tends to form carbon layer coating on the surface of TiO_2, instead of doping into internal TiO_2 lattice. However, it inevitably enters into the surface lattice of TiO_2 to play as an interstitial atom, considering the small atom size of C. We think that this type of C-doping existed in the interface between carbon layer and TiO_2 core, and this is also the reason for the decreased optical bandgap of C/TiO_2 as **Fig. 5** shown. In addition, the great difference value in ion radius between C^{4+} (16 pm) and Ti^{4+} (61 pm) would not lead C to play as a substitution of Ti in the TiO_2 matrix; meanwhile, the comparison of XP C 1s spectra of the samples is shown in Fig. S2 (a), and there is also no evidence that C atom substitutes O atom to occupy the TiO_2 lattice, because of no signal of Ti-C bonding occurred at ~282 eV [28]. XP Ti 2p spectra (Figure. S2(b)) of C/TiO_2 and reduced TiO_2 exhibit a shift of ~0.3 eV to high energy comparing with the reference TiO_2 sample, which indicate the presence of V_Os in these modified TiO_2' surface. Since V_O registers as positive charge (V_O^{2+}), each of

the three nearest-neighbor Ti atoms moves away from the vacancy toward its five remaining O neighbors. This causes the shortening in the Ti–O bond length, as well as the increase in bonding energy. Similarly, the fitted peaks of XPS O 1s spectra (Figure. S2(c)-(e)) illustrate that the "absorption O" (adsorbed O_2 /V_Os and adsorbed H_2O/OH groups) abounds in the surface of modified TiO_2 samples.

Fig. 6 (a), (b) and **(c)** show valence band XPS (VB-XPS) of the reference TiO_2, C/TiO_2 and reduced TiO_2 NPs, respectively. The reference TiO_2 displays the characteristic VB density of states (DOS) of TiO_2, with the band edge at about 1.23 eV below the Fermi energy. Since the optical bandgap of reference TiO_2 is 3.3 eV (**Table S1**), the conduction band minimum (CBM) would occur at -2.07 eV [19]. For the VB-XPS of both C/TiO_2 and reduced TiO_2 samples, a notable difference comparing with the reference TiO_2 sample is the presence of band tail induced by structural disorders. The main absorption onsets of C/TiO_2 and reduced TiO_2 samples are located at 1.06 and 1.19 eV, respectively, whereas the maximum energies associate with the band tails at about 0.22 and 0.27 eV, respectively. Therefore, their corresponding CBM should locate at -1.84 and -2.01 eV, respectively. Consequently, the remarkable bandgap narrowing of the modified samples (2.06 vs. 2.28 eV) are caused by the substantial shifts of VB tails, and the values would further decrease due to the predicted CB tailing [19].

Fig. 7 presents schematic NP's structure and corresponding calculated DOS (band edge) of three samples, which is built using the experimental data from the UV–Vis spectroscopy and VB-XPS results. The DOS band edge charts of the C/TiO_2 and reduced TiO_2 present a clear illustration of the reasonable bandgap narrowing to enhance the photocatalytic activity. The favorable water-splitting mechanism including the modified reduction and oxidation potentials of both C/TiO_2

and reduced TiO_2 is also displayed.

The significant bandgap engineering of the modified TiO_2 samples provides the improvement of photocatalytic activity based on the remark availability of solar energy. Moreover, the dislocations and the lattice distortion in the C/TiO_2 and reduced TiO_2 NPs act as electroactive defects to bring localized band bending. The band bending and the associated electric field in the space charge region can promote the separation of photogenerated electron/hole pair [29, 30]. For C/TiO_2 NPs, the carbon shell makes a further enhancement on inhibiting the electron/hole pair recombination or prolonging the lifetime of charge carriers, in comparison with the reduced TiO_2 NPs. In present work, the carbon shell is thin enough to allow light transmitting to the TiO_2 core and the surface $d-\pi$ conjugation structure of the C/TiO_2 NPs endows the photogenerated electrons to transfer from the conduction band of TiO_2 to carbon shell [16, 31]. Since the carbon shell possesses excellent conductivity of electrons [31, 32], the photogenerated electron/hole pair separate smoothly and then these carriers could rapidly go through the surface photo-oxidation reactions. This is the reason for the better degradation efficiency of C/TiO_2 comparing with that of reduced TiO_2 NPs.

A desirable photocatalyst to achieve high efficiency for hydrogen production through water-splitting should have a band gap around 2.0 eV (2.06 vs. 2.28 eV in our work), and the positions of its band edges must match with the redox potentials of water [33]. Furthermore, to modify TiO_2 to be a candidate for water splitting, it should not affect much of the CBM but increases the VBM significantly. In present work, the band structures of C/TiO_2 and reduced TiO_2 NPs have been modified to increase the VBM greatly, thus both modified samples perform obvious improvements of the efficiency of hydrogen production compared with the reference TiO_2 as shown in **Fig. 4(b)**. Notably, reduced TiO_2 NPs display a more excellent H_2 release rate, which is nearly

three times and 10 times higher than that of C/TiO_2 and reference TiO_2, respectively. From Figure 7, the CBM of reduced TiO_2 is higher than that of C/TiO_2, which means the reduction potential of reduced TiO_2 is bigger than that of C/TiO_2 in the water-splitting process. The difference in the reduction potential (0.07~0.17 eV vs. 0.24~0.34 eV) between them is 0.17 eV, i.e., the reduction potential of reduced TiO_2 is 0.17 eV higher than that of C/TiO_2. Meanwhile, the lower VBM of reduced TiO_2 also represents its higher oxidizing potential (0.05 eV) than that of C/TiO_2. As the optical response ranges of the modified samples are both extended to the visible light region, the reduced TiO_2 sample possesses much more favorable chemical potentials for water-splitting, thus it exhibits a more excellent efficiency in hydrogen production.

Conclusions

In summary, we have presented an economical and green one-step approach to synthesize core-shell C/TiO_2 nanocrystals with structural disorders, meanwhile the reduced TiO_2 with similar structural disorders have been obtained through decarburization process for C/TiO_2 NPs. The structural disorders in the catalysts induce the valence band tail to narrow the bandgap significantly and to tailor the band structure to adapt for the redox potentials of water in photocatalytic process. The unique morphology and structure enable both modified TiO_2 samples to possess visible response and outstanding photocatalytic activities. Having their respective merits, the C/TiO_2 NPs display better on photodegradation of water pollutants attributed to the rapid charge transfer of carbon shell; and the reduced TiO_2 performs a much better efficiency in H_2 production in consideration of its proper positions of band edges. The findings of our study may provide a facile way to develop nanostructural disordered TiO_2 photocatalyst to enhance the photocatalytic activity, to be applied both in water pollution treatment and the generation of clean energy source.

Acknowledgements

This work is supported by the Foundation of National Key Basic Research and Development Program (No.2010CB631001) and the Program for Changjiang Scholars and Innovative Research Team in University.

Reference

[1] A. Fujishima and K. Honda, Nature, 1972, **238**, 37-38.

[2] A. Fujishima, T. N. Rao and D. A. Tryk, J. Photochem. Photobiol. C, 2000, **1**,1-21.

[3] D. A. Tryk, A. Fujishima and K. Honda, Electrochim. Acta., 2000, **45**, 2363-2376.

[4] M. Grätzel, Nature, 2001, **414**, 338-344.

[5] A. Hagfeldt and M, Grätzel, Chem. Rev., 1995, **95**, 49-68.

[6] A. L. Linsebigler, G. Lu, and J. T. Yates. Jr, Chem. Rev., 1995, **95**,735-758.

[7] A. Millis and S. L. Hunte, J. Photochem. Photobiol. A, 1997, **108**,1-35.

[8] F. Zuo, L. Wang, T. Wu, Z. Y. Zhang, D. Borchardt and P. Y. Feng, J. Am. Chem. Soc., 2010, **132**, 11856-11857.

[9] G. Jiang, Z. Lin, C. Chen, L. Zhu, Q. Chang, N. Wang,W. Wei and H. Tang, Carbon, 2011, **49**, 2693–2701.

[10] D. Sarkar, C. K. Ghosh, S. Mukherjee and K. K. Chattopadhyay, ACS Appl. Mater. Interfaces, 2013, **5**, 331-337.

[11] Q. Xiang, J. Yu and M. Jaroniec, J. Am. Chem. Soc., 2012, **134**, 6575-6578.

[12] M. Murdoch, G. I. N. Waterhouse, M. A. Nadeem, J. B. Metson, M. A. Keane, R. F. Howe, J. Llorca and H. Idriss, Nat. Chem., 2011, **3**, 489-492.

[13] Y. Liang, H. Wang, H. S. Casalongue, Z. Chen, and H. Dai, Nano Res., 2010, **10**, 701-705.

[14] H. Zhang, X. Lv, Y. Li, Y. Wang and J. Li, ACS Nano., 2010, **4**, 380-386.

[15] G. Williams, B. Seger, and P. V. Kamat, ACS Nano., 2008, **2**, 1487-1491.

[16] L. W. Zhang, H. B. Fu, and Y. F. Zhu, Adv. Funct. Mater., 2008, **18**, 2180-2189.

[17] L. Zhao, X. Chen, X. Wang, Y. Zhang, W. Wei, Y. Sun, M. Antonietti and M. M. Titirici, Adv. Mater., 2010, **22**, 3317-3321.

[18] Y. Zhang, Z. Tang, X. Fu and Y. Xu, ACS Nano., 2010, **4**, 7303-7314.

[19] X. Chen, L. Liu, P. Y. Yu, and S. S. Mao, Science, 2011, **331**, 746-750.

[20] A. Naldoni, M. Allieta, S. Santangelo, M. Marelli, F. Fabbri, S. Cappelli, C. L. Bianchi, R. Psaro, and V. D. Santo, J. Am. Chem. Soc., 2012, **134**, 7600-7603.

[21] G. Wang, H. Wang, Y. Ling, Y. Tang, X. Yang, R. C. Fitzmorris, C. Wang, J. Z. Zhang, and Y. Li, Nano Lett., 2011, **11**, 3026-3033.

[22] X. Chen, L. Liu, Z. Liu, M. A. Marcus, W. C. Wang, N. A. Oyler, M. E. Grass, B. Mao, P. A. Glans, P. Y. Yu, J. Guo and S. S. Mao, Sci. Rep., 2013, **3**, 1510.

[23] X. Chen, X. and S. S. Mao, Chem. Rev., 2007, **107**, 2891-2959.

[24] D. H. Pearson, C. C. Ahn and B. Fultz, Phys. Rev. B, 1993, **47**, 8471-8478.

[25] J. H. Paterson and O. L. Krivanek, Ultramicroscopy, 1990, **32**, 319-325.

[26] C. D. Valentin, and G. Pacchioni, J. Phys. Chem. C, 2009, **113**, 20543-20552.

[27] E. Finazzi, C. D. Valentin, G. Pacchioni, and A. Selloni, J. Chem. Phys., 2008, **129**, 154113.

[28] L. Zhang and R. V. Koka, Mater. Chem. Phys., 1998, **57**, 23-32.

[29] D. M. Adams, L. Brus, C. E. D. Chidsey, S. Creager, C. Creutz, C. R. Kagan, P. V. Kamat, M. Lieberman, S. Lindsay, R. A. Marcus, R. M. Metzger, M. E. Michel-Beyerle, J. R. Miller, M. D. Newton, D. R. Rolison, O. Sankey, K. S. Schanze, J. Yardley and X. Zhu, J. Phys. Chem. B, 2003, **107**, 6668-6697.

[30] J. B. Asbury, E. Hao, Y. Wang, H. N. Ghosh and T. Lian, J. Phys. Chem. B, 2001, **105**, 4545-4557.

[31] X. Wang, L. Zhi and K. Müllen, Nano Lett., 2008, **8**, 323-327.

[32] K. S. Novoselov, A. K. Geim, S. V. Morozov, D. Jiang, Y. Zhang, S. V. Dubonos, I. V. Grigorieva and A. A.

Firsov, Science, 2004, **306**, 666-669.

[33] O. Khaselev and J. A. Turner, Science, 1998, **280**, 425-427.

Graphical Abstract:

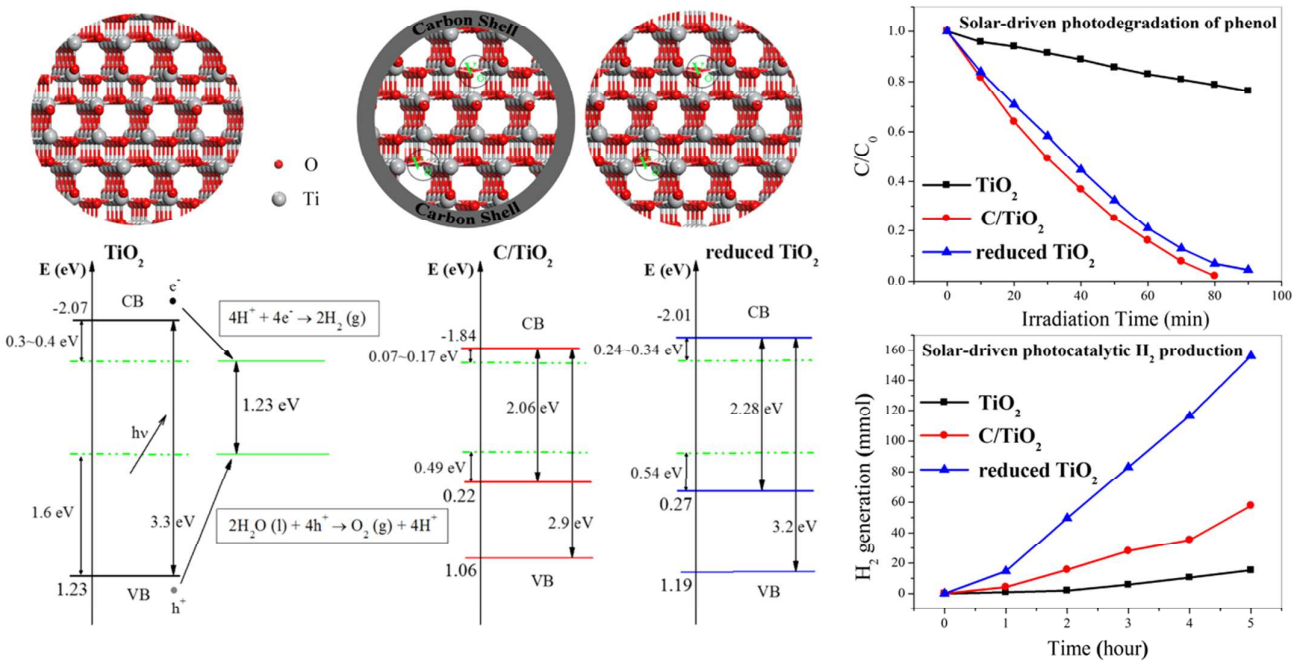

This paper summarizes the applications of V_Os-induced structural disorders of core-shell C/TiO_2 and reduced TiO_2 on improving the solar-driven photocatalytic activities.

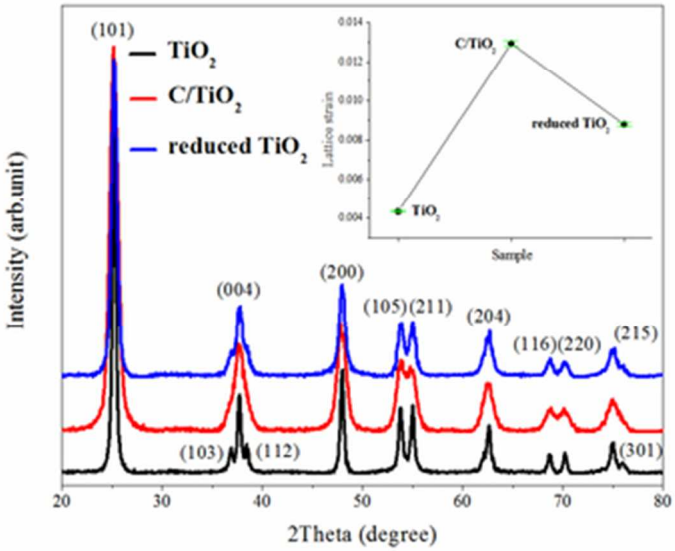

Fig. 1 XRD patterns of the three TiO2 samples, the comparison of their lattice strain is shown in the insert.
16x13mm (600 x 600 DPI)

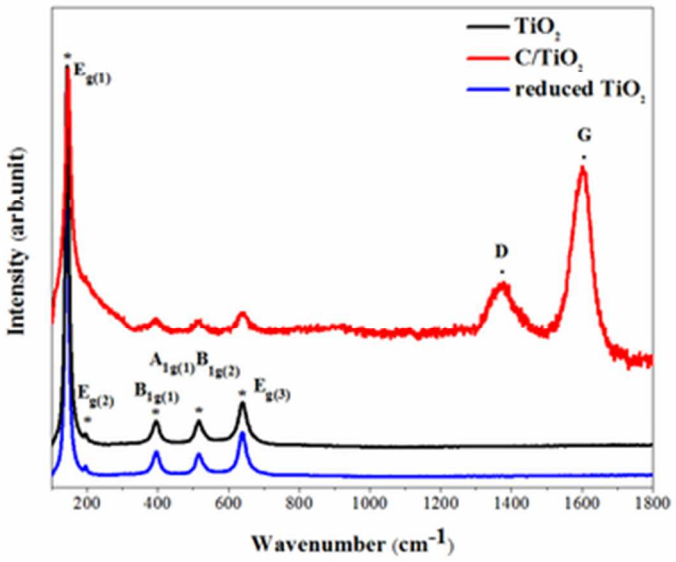

Fig. 2 Raman spectra of the reference TiO2, C/TiO2 and reduced TiO2 NPs.
16x13mm (600 x 600 DPI)

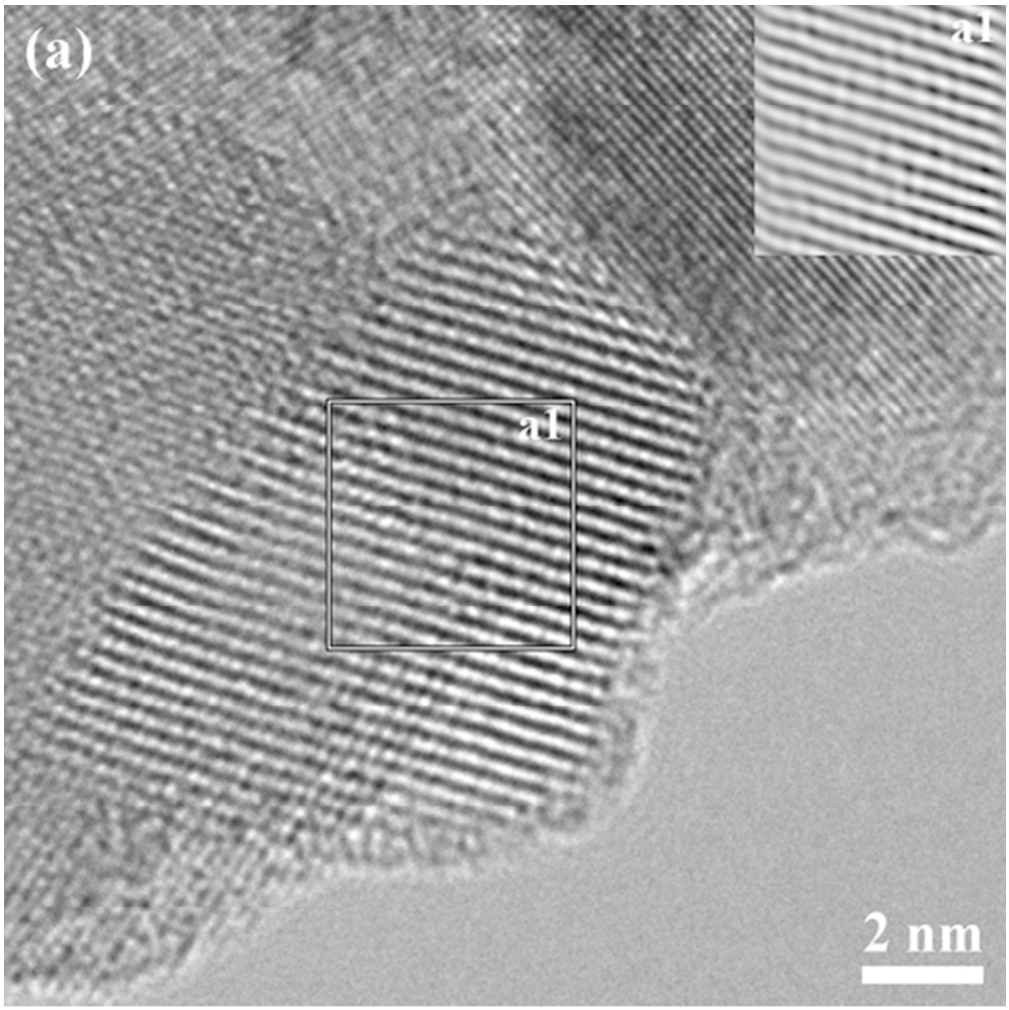

Fig. 3(a) HRTEM micrograph of reference TiO2, along with its Fourier-filtered image (a1) of the selected area.
43x43mm (300 x 300 DPI)

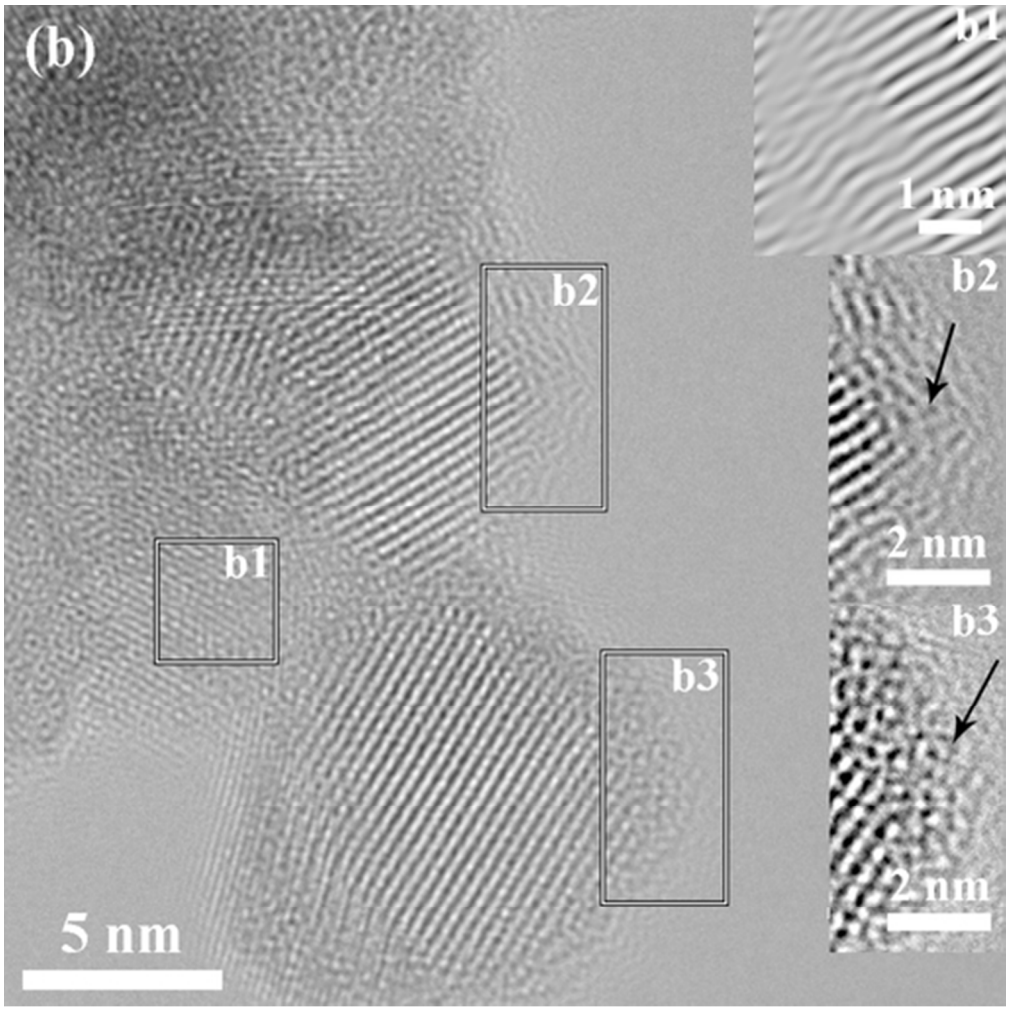

Fig. 3(b) HRTEM micrograph of C/TiO2, along with its Fourier-filtered image (b1) of the selected area and the local enlarged images (b2 and b3) shown as the insets.
43x43mm (300 x 300 DPI)

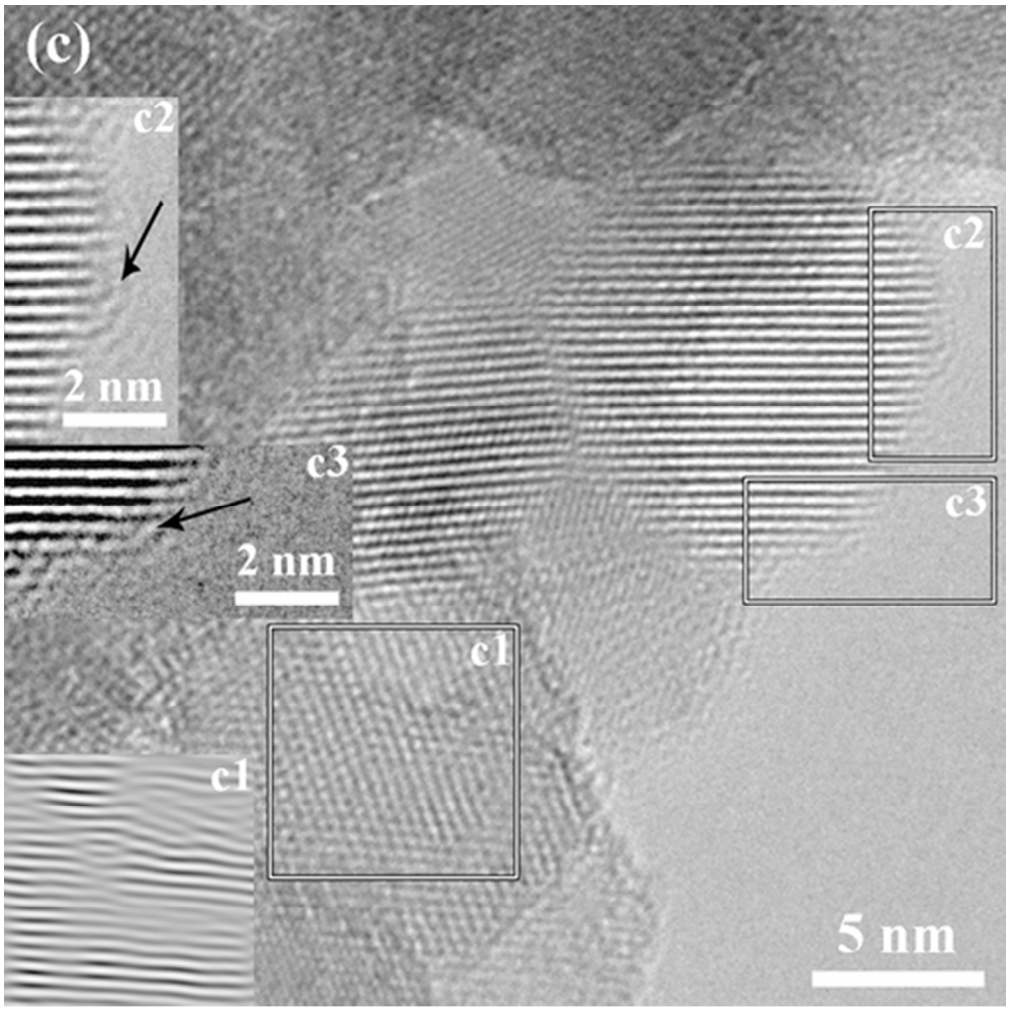

Fig. 3(c) HRTEM micrograph of reduced TiO2, along with its Fourier-filtered image (c1) of the selected area and the local enlarged images (c2 and c3) shown as the insets.
43x43mm (300 x 300 DPI)

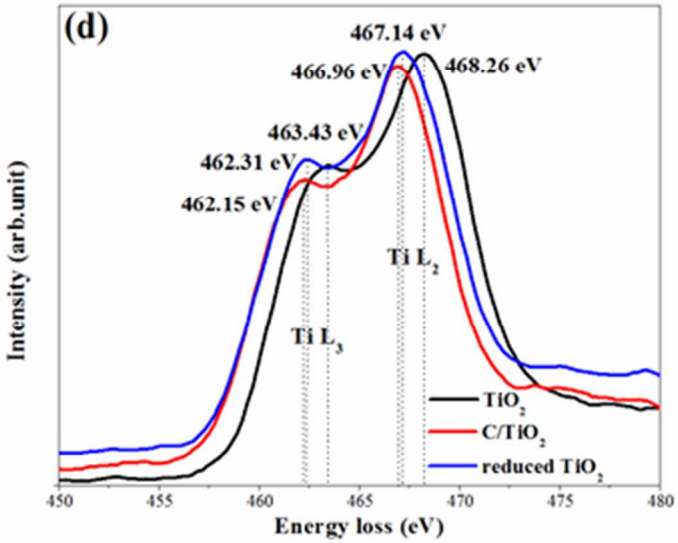

Fig. 3(d) EELS spectra of the Ti–L2,3 edge for the three samples.
16x13mm (600 x 600 DPI)

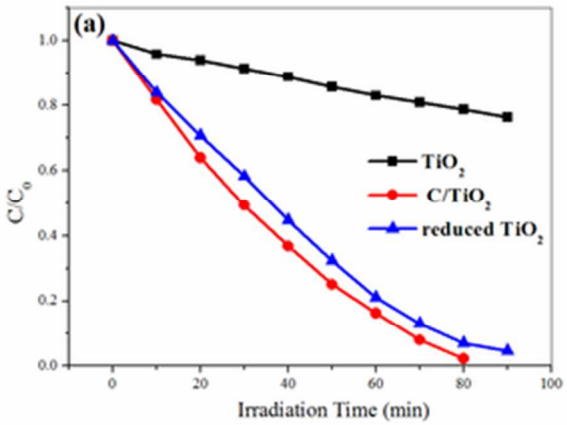

Fig. 4 Comparison of the simulated solar-driven photocatalytic activities of the reference TiO2, C/TiO2 and reduced TiO2 nanocrystals under the same experimental conditions. (a) Phenol decomposition with time of the three samples.
14x10mm (600 x 600 DPI)

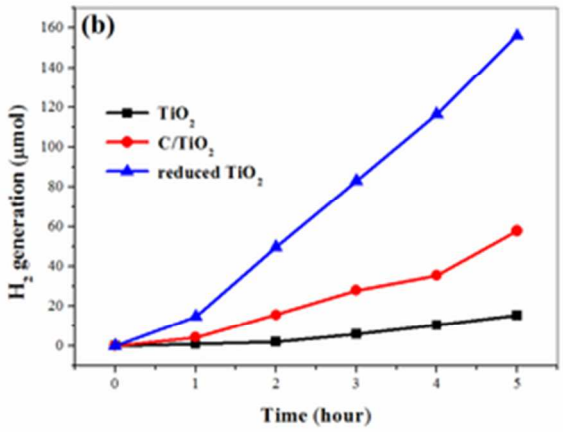

Fig. 4 Comparison of the simulated solar-driven photocatalytic activities of the reference TiO2, C/TiO2 and reduced TiO2 nanocrystals under the same experimental conditions. (b) Hydrogen (H2) generation with time of the three samples.
14x10mm (600 x 600 DPI)

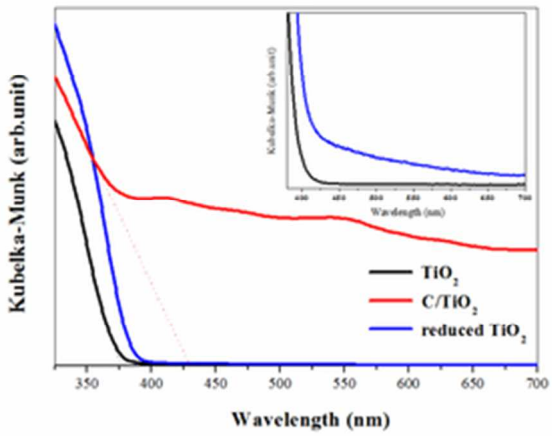

Fig. 5 UV-visible diffuse reflectance spectra of the three samples and the detailed comparison between reference TiO2 and reduced TiO2 is shown as an insert.
14x10mm (600 x 600 DPI)

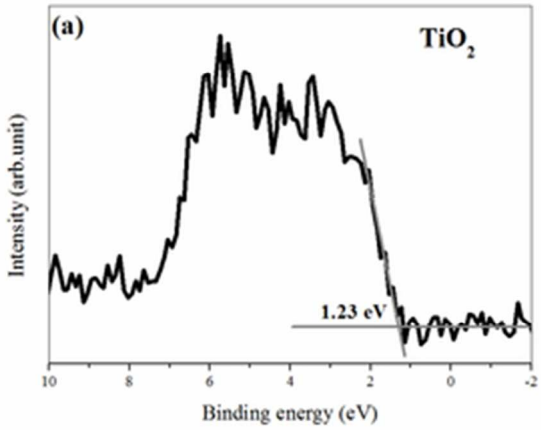

Fig. 6(a) Valence band XPS spectrum of reference TiO2. The gray auxiliary lines show the linear extrapolation of the curve used for deriving the band edge position of the sample.
14x10mm (600 x 600 DPI)

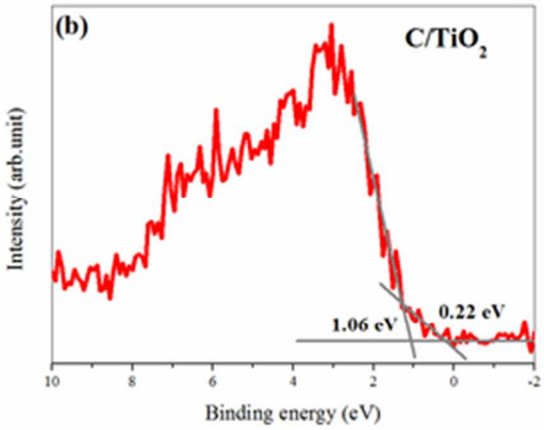

Fig. 6(b) Valence band XPS spectrum of C/TiO2. The gray auxiliary lines show the linear extrapolation of the curve used for deriving the band edge position of the sample.
14x10mm (600 x 600 DPI)

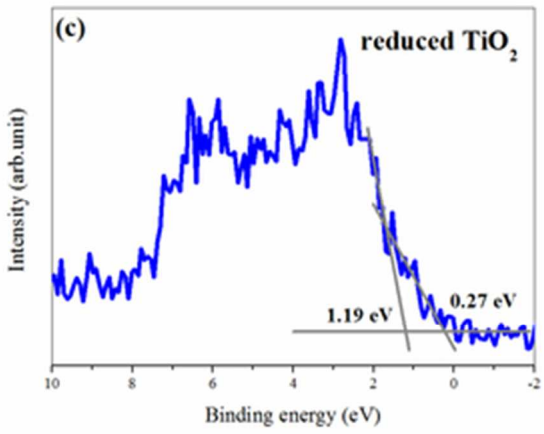

Fig. 6(c) Valence band XPS spectrum of reduced TiO2. The gray auxiliary lines show the linear extrapolation of the curve used for deriving the band edge position of the sample.
14x10mm (600 x 600 DPI)

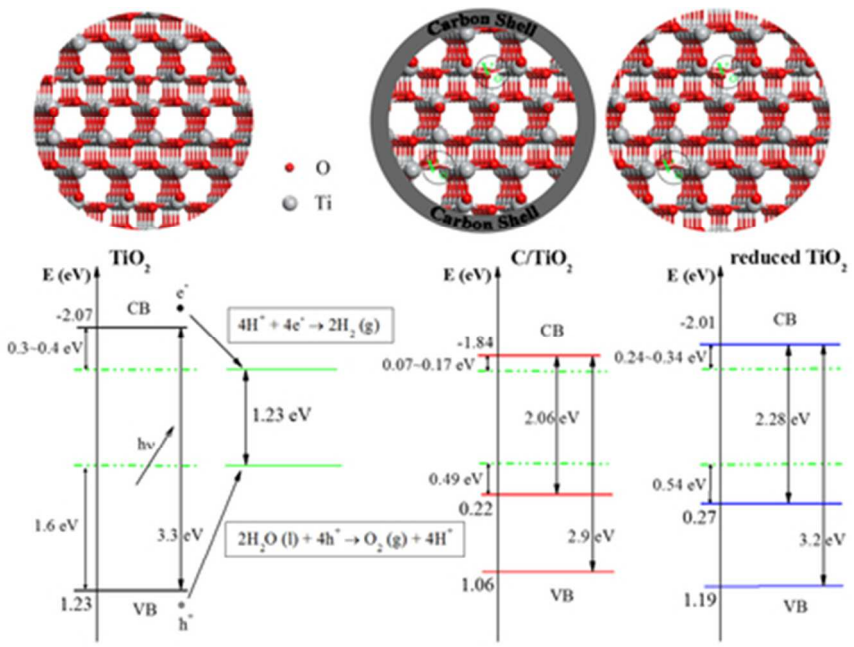

Fig. 7 Schematic illustrations of the nanostructures and the calculated DOSs based on the UV-visible diffuse reflectance spectra and the VB-XPS results, for the reference TiO2, C/TiO2 and reduced TiO2, respectively. The energy for the valence band maximum of the bulk phase is taken to be zero.
37x27mm (300 x 300 DPI)

Fig. 1 XRD patterns of the three TiO_2 samples, the comparison of their lattice strain is shown in the insert.

Fig. 2 Raman spectra of the reference TiO_2, C/TiO_2 and reduced TiO_2 NPs.

Fig. 3 HRTEM micrographs of **(a)** reference TiO_2, **(b)** C/TiO_2 and **(c)** reduced TiO_2, respectively, along with their Fourier-filtered images **(a1, b1, c1)** of the selected area and the local enlarged images (**b2, b3** and **c2, c3**) shown as the insets. **(d)** EELS spectra of the Ti–$L_{2,3}$ edge for the three samples.

Fig. 4 Comparison of the simulated solar-driven photocatalytic activities of the reference TiO_2, C/TiO_2 and reduced TiO_2 nanocrystals under the same experimental conditions. **(a)** Phenol decomposition with time of the three samples. **(b)** Hydrogen (H_2) generation with time of the three samples.

Fig. 5 UV-visible diffuse reflectance spectra of the three samples and the detailed comparison between reference TiO_2 and reduced TiO_2 is shown as an insert.

Fig. 6 Valence band XPS spectra of **(a)** reference TiO_2, **(b)** C/TiO_2 and **(c)** reduced TiO_2, respectively. The gray auxiliary lines show the linear extrapolation of the curves used for deriving the band edge position of these samples.

Fig. 7 Schematic illustrations of the nanostructures and the calculated DOSs based on the UV-visible diffuse reflectance spectra and the VB-XPS results, for the reference TiO_2, C/TiO_2 and reduced TiO_2, respectively. The energy for the valence band maximum of the bulk phase is taken to be zero.